INTERNATIONAL JOURNAL FOR NUMERICAL METHODS IN FLUIDS
Int. J. Numer. Meth. Fluids 2008; **58**:527–549
Published online 18 February 2008 in Wiley InterScience (www.interscience.wiley.com). DOI: 10.1002/fld.1757

Sliding mesh algorithm for CFD analysis of helicopter rotor–fuselage aerodynamics

R. Steijl and G. Barakos*,†

Laboratory of Computational Fluid Dynamics, Department of Engineering, University of Liverpool, Liverpool L69 3GH, U.K.

SUMMARY

The study of rotor–fuselage interactional aerodynamics is central to the design and performance analysis of helicopters. However, regardless of its significance, rotor–fuselage aerodynamics has so far been addressed by very few authors. This is mainly due to the difficulties associated with both experimental and computational techniques when such complex configurations, rich in flow physics, are considered. In view of the above, the objective of this study is to develop computational tools suitable for rotor–fuselage engineering analysis based on computational fluid dynamics (CFD).

To account for the relative motion between the fuselage and the rotor blades, the concept of sliding meshes is introduced. A sliding surface forms a boundary between a CFD mesh around the fuselage and a rotor-fixed CFD mesh which rotates to account for the movement of the rotor. The sliding surface allows communication between meshes. Meshes adjacent to the sliding surface do not necessarily have matching nodes or even the same number of cell faces. This poses a problem of interpolation, which should not introduce numerical artefacts in the solution and should have minimal effects on the overall solution quality. As an additional objective, the employed sliding mesh algorithms should have small CPU overhead. The sliding mesh methods developed for this work are demonstrated for both simple and complex cases with emphasis placed on the presentation of the inner workings of the developed algorithms. Copyright © 2008 John Wiley & Sons, Ltd.

Received 8 August 2007; Revised 18 December 2007; Accepted 19 December 2007

KEY WORDS: sliding planes; mesh deformation; rotorcraft CFD; rotor–fuselage interaction

1. INTRODUCTION

The study of rotor and rotor–fuselage aerodynamics with computational fluid dynamics (CFD) methods, based on structured grids, requires complex multi-block topologies so that the exact

*Correspondence to: G. Barakos, Department of Engineering, University of Liverpool, Chadwick Building, Liverpool L69 3GH, U.K.
†E-mail: g.barakos@liverpool.ac.uk

Contract/grant sponsor: European Union; contract/grant number: 516074

shapes of the rotor blades and helicopter fuselage are represented. An additional difficulty stems from the requirement to account for the relative motion between the rotor blades and the relative motion between the rotor and the fuselage. In this paper, the concept of sliding grids with non-matching cell faces is used to allow multi-block-structured grid solvers to cope with rotor–fuselage flow cases. Figure 1 shows an example of multi-block structured fuselage and rotor meshes which have non-matching topologies along the sliding-mesh interface separating the two domains. The concept of non-matching cell faces is not new in CFD and has so far been used by many researchers. References [3, 4], amongst others, present the fundamentals of interface conditions for non-matching cell faces. Such methods are nowadays common in turbo-machinery [5], where non-matching and rotating cell faces are used for the simulation of the flow between adjacent blade-rows of aero engines.

Reference [3] introduced a conservative 'zonal' or 'patched-grid' approach in which two-dimensional flow calculations are performed on grids patched at zonal interfaces. A conservative scheme was obtained by constructing the flux through a cell face along the zonal boundary via a weighted summation of the fluxes through the various parts contributing to each cell face. A piece-wise constant variation of the numerical flux was used with a first-order accurate spatial discretization of Euler's equations. The flux computation was based on either Osher's scheme [6]

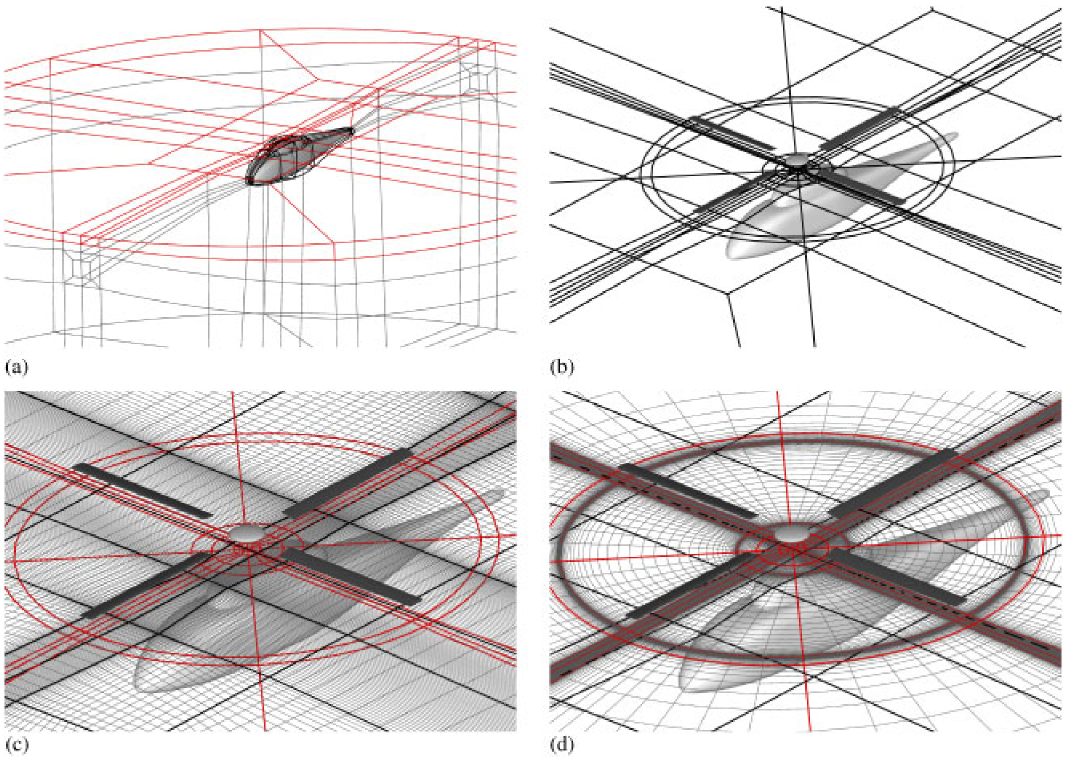

Figure 1. Application example of sliding meshes for rotor–fuselage configurations: (a) multi-block topology around the fuselage (ROBIN body [1, 2]); (b) multi-block topology on both sides of the sliding-plane interface; (c) fuselage mesh on the sliding plane; and (d) rotor mesh on the sliding plane. The differences in mesh topology and density between (c) and (d) are apparent.

or the split-flux method of Steger and Warming [7]. First-order accurate explicit time integration was employed. The method was applied to a range of two-dimensional test cases composed of the supersonic flow over a cylinder, blast-wave diffraction by a wedge and the shock-tube problem. The test cases involved a range of Cartesian as well as curvilinear meshes. For the cylinder test case, a curved zonal interface was used. A detailed analysis showed that for the scheme in Reference [3], a drift in the free stream conditions occurs near this curved zonal boundary which is proportional to the curvature of the zonal boundary and is caused by terms that are second order in magnitude. The presented results indicated that the conservative nature of the method permits the smooth transition of the discontinuities in the considered flow fields across the zonal boundaries. In Reference [4], the approach was extended to include relative motion between grid patches. Furthermore, the method was demonstrated to work with an implicit relaxation method, for steady-state and time-accurate simulations. A time-dependent simulation of a rotor–stator configuration was also presented, demonstrating the method for time-dependent flows. The formulation and the presented results were restricted to two-dimensional cases. The approach of References [3, 4] was subsequently adopted by various researchers and extended to three-dimensional problems. An example of such efforts can be found in Reference [5], where multi-blade row configurations of gas turbines are analysed using RANS simulations on unstructured CFD meshes with sliding surfaces forming the interfaces between the mesh parts with relative motion. In Reference [8], the sliding-surface approach was employed for three-dimensional Euler calculations on structured meshes for propellers and propeller-wing configurations.

In the context of rotorcraft CFD, the CHIMERA technique is established as the standard for dealing with the relative motion of the rotor blades (due to the cyclic blade pitch actuation as well as blade flapping) and the relative motion between the rotor and the helicopter fuselage. This method allows intersecting and non-matching grids and is therefore more general than the sliding-surface approach. Examples of applications to rotorcraft problems are given in References [9–12] amongst others. In these works, a separate block-structured mesh is utilized for each rotor blade overlaying a highly regular, structured background grid. A ‘hole-cutting’ approach is used at each time step to determine the parts of the domain that are covered by overlapping grids and to create a suitable amount of overlap between them. Halo cells are utilized to couple the solution between grids. The required search and interpolation steps need to be conducted in a three-dimensional space. For rotor–fuselage configurations, e.g. in References [10, 12], an additional block-structured mesh for the fuselage must be used. For this case, additional complexity in the hole-cutting and interpolation steps may arise when a three-fold grid overlap occurs, i.e. in certain parts of the domain, the background, rotor blade and fuselage grids will overlap.

In this work, the sliding-mesh approach with non-matching cell faces is considered, in an effort to develop a computational technique that allows rotor body as well as complex rotor cases to be studied with minimal overhead and by re-using existing multi-block grids. In contrast to the large number of CHIMERA applications in rotorcraft CFD, only a limited number of applications of the sliding-mesh approach exist. In References [13, 14], an unstructured Euler solver is described utilizing sliding planes to couple the mesh around the rotor with a stationary mesh around a helicopter fuselage. The grid deformation due to the relative motion of the rotor blades is taken into account by utilizing a mesh deformation algorithm based on the spring analogy. Further application and validation of the same algorithm has also been presented in Reference [15].

In view of the above, the objectives of the present work are the development of a sliding-mesh algorithm, its implementation in a well-validated finite-volume CFD method and its demonstration for a wide range of test cases ranging from simple aerofoils to full rotor–fuselage configurations.

The paper begins with a description of the employed solver in Section 2, and subsequently, the sliding-mesh algorithms are detailed in Section 3. Section 4 presents demonstration test cases and Section 5 presents conclusions and suggests future steps. With respect to structured multi-block grids, this work is the first to address sliding planes for rotor–fuselage applications.

2. NUMERICAL METHOD

2.1. The HMB flow solver

The helicopter multi-block (HMB) CFD code [16–18] was employed for this work. HMB solves the unsteady Reynolds-averaged Navier–Stokes equations on block-structured grids using a cell-centred finite-volume method for spatial discretization. Implicit time integration is employed, and the resulting linear systems of equations are solved using a pre-conditioned generalized conjugate gradient method [19]. For unsteady simulations, an implicit dual time-stepping method is used, based on Jameson's pseudo-time-integration approach [20]. The method has been validated for a wide range of aerospace applications and has demonstrated good accuracy and efficiency for very demanding flows. Examples of work with HMB can be found in References [16–18, 21, 22] and include dynamic stall [22], blade–vortex interaction [21] and rotors in hover and forward flight [17]. Several rotor trimming methods are available in HMB along with a blade-actuation algorithm that allows for the near-blade grid quality to be maintained on deforming meshes [17]. The same algorithm is used here for the mesh deformation of the rotor mesh. The solver has a library of turbulence closures which includes several one- and two-equation turbulence models and even non-Boussinesq versions of the k–ω model. Turbulence simulation is also possible using either the large-eddy or the detached-eddy approach. The HMB solver was designed with parallel execution in mind. The MPI library along with a load-balancing algorithm is used to this end. Good parallel performance has been demonstrated on Beowulf clusters with up to 150 CPUs and on massively parallel machines such as the HPCx facility available to U.K. Universities. For multi-block grid generation, the ICEM-CFD Hexa commercial meshing tool is used and CFD grids with multi-million points and thousands of blocks are commonly used with the HMB solver.

Two layers of halo cells are used in the HMB solver for imposing boundary conditions or to allow communication between adjacent blocks. Figure 2(a) presents a schematic of this arrangement. Each block is independent of its neighbouring blocks, and as long as the halo cells are populated with values of the primitive variables, the solver can compute an update of the flow solution.

2.2. Governing equations in inertial frame of reference

The Navier–Stokes equations expressed in integral form in the arbitrary Lagrangian Eulerian formulation for time-dependent domains, which may include moving boundaries, read

$$\frac{\mathrm{d}}{\mathrm{d}t}\int_{V(t)} \mathbf{w}\,\mathrm{d}V + \int_{\partial V(t)} (\mathbf{F}(\mathbf{w}) - \mathbf{F}_v(\mathbf{w}))\mathbf{n}\,\mathrm{d}S = \mathbf{S} \tag{1}$$

The above forms a system of conservation laws for any time-dependent control volume $V(t)$ with boundary $\partial V(t)$ and outward unit normal $\mathbf{n}$. The vector of conserved variables is denoted by $\mathbf{w} = [\rho, \rho u, \rho v, \rho w, \rho E]^{\mathrm{T}}$, where ρ is the density, u, v, w are the Cartesian velocity components and E is the total internal energy per unit mass. $\mathbf{F}$ and $\mathbf{F}_v$ are the inviscid and viscous fluxes,

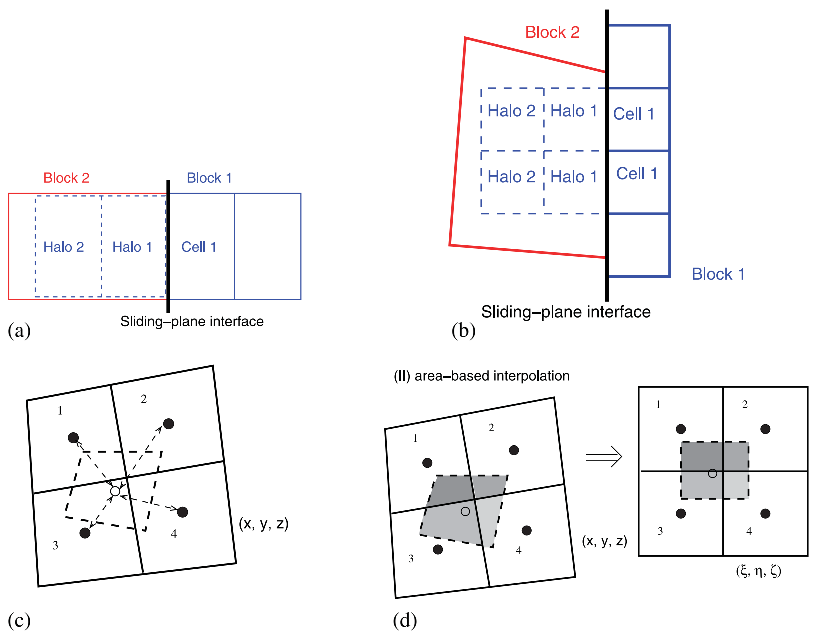

Figure 2. Sliding-plane interface with matching and non-matching cell faces: (a) halo cells and matching cells; (b) non-matching cells along the interface; (c) sketch of distance-based interpolation; and (d) sketch of cell-area weighted interpolation.

respectively. The fluxes include the effect of the time-dependent domain, i.e. a mesh velocity is included in the contra-variant velocity components. In the absence of volume forces and in an inertial frame of reference, the source term $\mathbf{S}=0$.

2.3. Spatial discretization

Equation (1) is discretized using a cell-centred finite-volume approach on structured multi-block grids which leads to a set of ordinary differential equations in time of the form

$$\frac{\partial}{\partial t}(\mathbf{w}_{i,j,k}V_{i,j,k}) = -\mathbf{R}_{i,j,k}(\mathbf{w}_{i,j,k}) \tag{2}$$

where $\mathbf{w}$ and $\mathbf{R}$ are the vectors of cell variables and residuals, respectively. Here, i,j,k are the cells indices in each block and $V_{i,j,k}$ is the cell volume. The convective terms are discretized using Osher's upwind scheme [6]. MUSCL variable interpolation is used to provide third-order accuracy with the Van Albada limiter [23] to prevent spurious oscillations near steep gradients. Boundary conditions are imposed by using two layers of halo cells around each grid sub-domain. In case of matching multi-block grids, the internal block boundaries are treated by copying flow field data from the two layers of boundary cells of the neighbouring block into the halo cells. At far-field boundary conditions, the flow field variables in the halo cells are simply set to the prescribed far-field condition. For inviscid flow simulations, solid-wall boundary conditions employ an extrapolation of the flow field variables from the interior to the halo cells such that the normal component of the velocity relative to the solid wall is zero. Similarly, for viscous flow simulations, halo cell values are extrapolated at solid boundaries ensuring that the velocity takes on any wall velocity.

2.4. *Temporal integration and the dual time-stepping method*

For time-accurate simulations, temporal integration is performed using an implicit dual time-stepping method. Following the pseudo-time formulation [20], the updated mean flow solution is calculated by solving the steady-state problems

$$\mathbf{R}^*_{i,j,k} = \frac{3V^{n+1}_{i,j,k}\mathbf{w}^{n+1}_{i,j,k} - 4V^{n}_{i,j,k}\mathbf{w}^{n}_{i,j,k} + V^{n-1}_{i,j,k}\mathbf{w}^{n-1}_{i,j,k}}{2\Delta t} + \mathbf{R}_{i,j,k}(\mathbf{w}^{n+1}_{i,j,k}) = 0 \tag{3}$$

where $V^{n-1}_{i,j,k}$, $V^{n}_{i,j,k}$ and $V^{n+1}_{i,j,k}$ represent the cell volumes at different time steps. Equation (3) represents a nonlinear system of equations. This system can be solved by introducing an iteration through *pseudo-time* τ to the steady state, as given by

$$\underbrace{V^{n+1}_{i,j,k}\frac{\mathbf{w}^{n+1,m+1}_{i,j,k} - \mathbf{w}^{n+1,m}_{i,j,k}}{V^{n+1}_{i,j,k}\Delta\tau}}_{A} + \frac{3V^{n+1}_{i,j,k}\mathbf{w}^{n+1,m}_{i,j,k} - 4V^{n}_{i,j,k}\mathbf{w}^{n}_{i,j,k} + V^{n-1}_{i,j,k}\mathbf{w}^{n-1}_{i,j,k}}{2V^{n+1}_{i,j,k}\Delta t} + \frac{\mathbf{R}_{i,j,k}(\mathbf{w}^{n+1,m}_{i,j,k})}{V^{n+1}_{i,j,k}} = 0 \tag{4}$$

where the mth pseudo-time iterate at real time step $n+1$ is denoted by $\mathbf{w}^{n+1,m}$ and the cell volumes are constant during the pseudo-time iteration. The unknown $\mathbf{w}^{n+1}_{i,j,k}$ is obtained when term A in Equation (4) converges to a specified tolerance. An implicit scheme is used for the pseudo-time integration. The flux residual $\mathbf{R}_{i,j,k}(\mathbf{w}^{n+1}_{i,j,k})$ is linearized as

$$\begin{aligned}\mathbf{R}_{i,j,k}(\mathbf{w}^{n+1}) &= \mathbf{R}_{i,j,k}(\mathbf{w}^{n}_{i,j.k}) + \frac{\partial \mathbf{R}_{i,j,k}(\mathbf{w}^{n}_{i,j.k})}{\partial t}\Delta t + O(\Delta t^2)\\ &\approx \mathbf{R}^{n}_{i,j,k}(\mathbf{w}^{n}_{i,j.k}) + \frac{\partial \mathbf{R}^{n}_{i,j,k}}{\partial \mathbf{w}^{n}_{i,j,k}}(\mathbf{w}^{n+1}_{i,j,k} - \mathbf{w}^{n}_{i,j,k})\end{aligned} \tag{5}$$

Using this linearization in pseudo-time, Equation (4) becomes a system of linear equations. For the solution of this system, the generalized conjugate gradient method with a block incomplete lower–upper pre-conditioner is used. Typically, the pseudo-time integration in Equation (4) is continued at each real time step until the residual has dropped three orders of magnitude.

3. SLIDING-MESH ALGORITHM

The underlying idea behind the sliding-mesh approach can be explained using the schematics of Figure 2. Figure 2(a) shows the definition of two layers of halo cells around the boundary surface of each block. In the sliding-plane algorithm, this concept is extended to deal with grids that are discontinuous across the interface and can also be in relative motion. Figure 2(b) presents a situation where two adjacent blocks have non-matching cell faces. If the halo cells of each block could, however, be populated with interpolated values, the solver will have no difficulty in computing the flow. The application of the sliding-plane algorithm to non-matching grids as well as grids in relative motion will result in non-matching cell faces as sketched in Figure 2(b). For each pair of adjacent sliding planes, there are three main steps involved in populating the halo cells: (i) identification of the neighbouring cells for each halo cell, (ii) interpolation of the solution at the centroids of the halo cells and (iii) exchange of information between blocks associated with different processors. The last step is important for computations on distributed-memory machines only. Regardless of the identification and interpolation methods employed, the halo-cell values are computed using

$$\phi_{\text{halo}} = \sum_{i=1}^{i=n} w_i \phi_i \tag{6}$$

where ϕ represents any flow field variable, e.g. $\rho, \rho u_i, \ldots, p$, etc., w_i is the weight associated with the ith neighbour of the halo cell and n is the number of neighbours.

Figures 2(c) and (d) show two possible methods used to determine the halo-cell values when neighbouring grids along a sliding-plane interface are discontinuous and may be in relative motion. The distance-based interpolation (shown in Figure 2(c)) computes a weighted sum of flow field data of neighbouring cells within an interaction radius. The weights are inversely proportional to the distance of the cell centre from the projected point on the sliding plane interface and are scaled to sum up to one. Figure 2(d) shows the cell-face overlap interpolation, in which case the weight for each neighbour is directly proportional to the fraction of the projected overlapping cell face area. In the context of finite-volume discretization methods for conservation laws based on numerical fluxes through cell faces, the cell-face overlap interpolation is the preferred method. However, an interpolation method based on the overlap weighting of Figure 2(d) does not necessarily enforce conservation and differences in grid sizes between the sides of the sliding plane may act as a spatial filter.

3.1. Interpolation method based on overlapping areas

The present implementation of the sliding-mesh algorithm is based on the cell-face overlap interpolation method presented in Figure 2(d). Sliding-mesh interfaces can be of arbitrary shape and for this reason the contributing cell surfaces must all be projected on the curvilinear ξ, η, ζ axes used in the solver. This step can be combined with a transformation from primitive to conservative variables so that flux-weighted summations can also be computed.

Figure 3 presents the underlying idea of the cell-face overlap interpolation used in the present sliding-mesh algorithm. The figure shows two adjacent non-matching meshes that are separated by the sliding-mesh interface. For both meshes, two layers of halo cells are constructed. Figure 3(a) shows how the first layer of halo cells of mesh 1 is obtained. At first, the face of each boundary cell in mesh 1 is projected onto the sliding-plane interface. Subsequently, the neighbour cells contributing to the halo data are identified. These cells belong to mesh 2 and their faces overlap the projected cell face from mesh 1. In the figure, three neighbours are shown. The interpolation weight assigned to each neighbour is the fraction of the projected cell face area occupied by the overlapping area of the two cells. For the second layer of halo cells of mesh 1, the procedure is presented in Figure 3(b). In this case, the face of the cell in mesh 1 is projected onto a plane formed by the cell faces one cell size away from the block boundary. The neighbours are now searched for in the second layer of cells below the block boundary of mesh 2. The present method assumes that the mesh spacing in the direction normal to the sliding-mesh interface is comparable in the adjacent grids.

If, in combination with the identification method, a regular intermediate surface grid is used to discretize the sliding plane, the interpolation method may also benefit. In this way, consistent interpolation on both sides of the sliding plane can be achieved. Figure 4 presents the cell-face

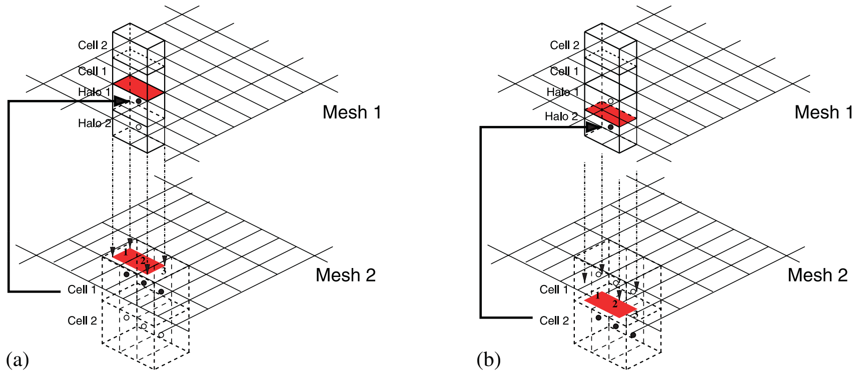

Figure 3. Sliding-plane algorithm employing 'direct' interpolation. The cell face is projected on the sliding-mesh interface. The cell-face overlap determines the interpolation weight for each of the donor cells: (a) first and (b) second layers of halo cells (mesh 1).

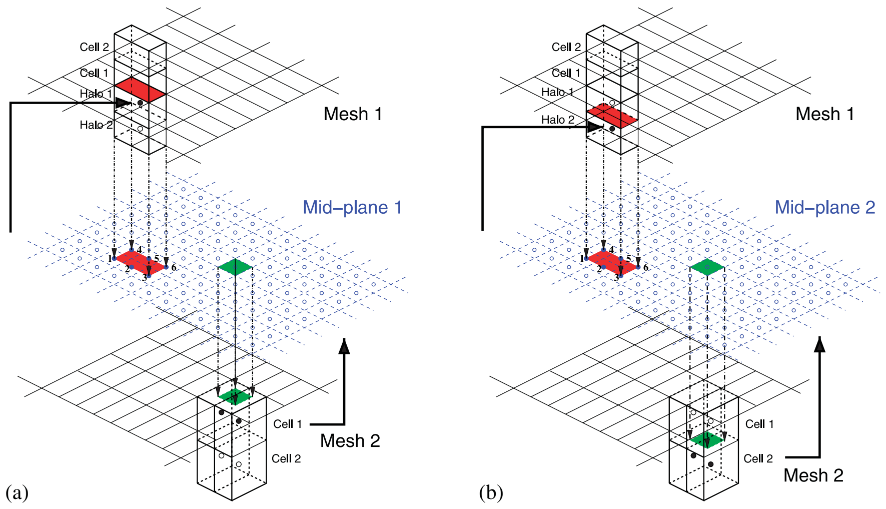

Figure 4. Sliding-plane algorithm employing 'mid-plane' interpolation. Four regularly spaced mid-planes are created with a mesh width smaller than the mesh spacing on either side of the sliding-mesh interface. First, mid-planes 1 and 2 are defined with data from the solution on mesh 2. These data are then used to define halo cell layers 1 (a) and 2 (b) of mesh 1.

overlap interpolation using a regular intermediate plane. The cell spacing of this intermediate plane needs to be smaller than the cell width on both sides of the sliding-plane interface. Combined with the need for regularity, this method requires the storage of a large number of intermediate cell values for large meshes with significant mesh stretching. Despite the benefits of the regularity of the intermediate-mesh interpolation in terms of identification efficiency and interpolation consistency, there is a significant memory overhead.

3.2. Identification of cell neighbours

Figure 5 shows the identification of neighbouring cells on a cylindrical sliding-plane interface between an inner grid around a blunt-nosed cylinder and a coarser (rotating) outer grid. As an example of the neighbour identification step, Figure 5(a) shows how cells on one of the block faces of the sliding-plane interface and on the inner mesh overlap with cells of the outer mesh. For the cell in the outer mesh indicated with shading in Figure 5(b), the six overlapping cell faces are shown. Similarly, Figure 5(c) shows the two neighbours on the outer grid for a cell on the inner sliding plane.

The neighbour identification method used in the present work involves a loop over all block faces on the sliding-plane interface(s). First, for each block face on the sliding-plane interface, a subset of block faces is constructed which are sufficiently close to have an overlap. To this end,

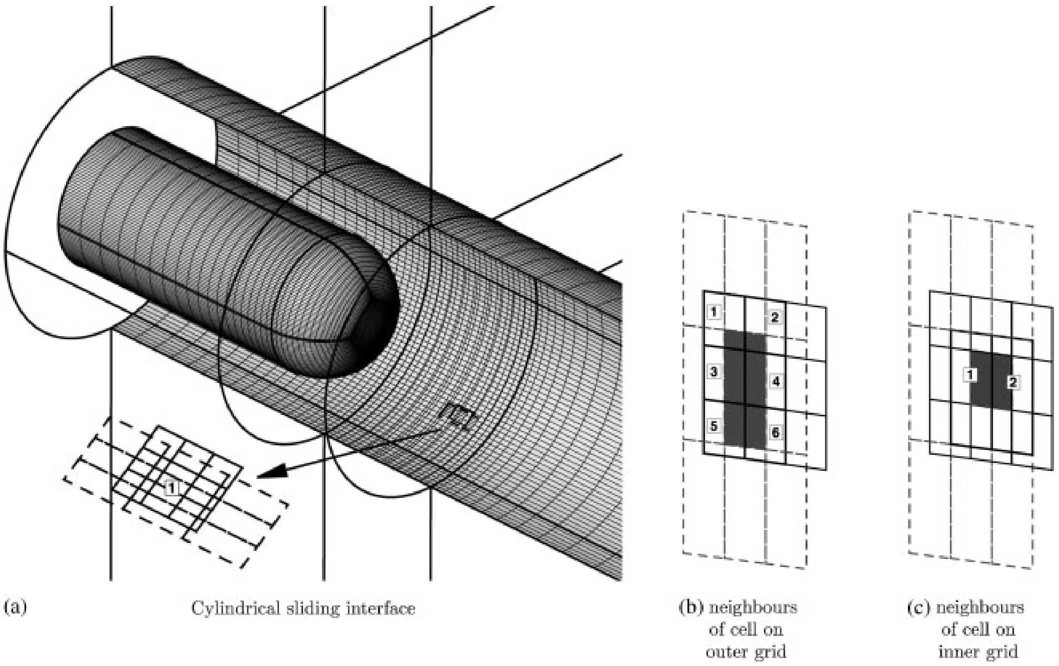
1
(a) Cylindrical sliding interface
1
2
3
4
5
6
(b) neighbours of cell on outer grid
1
2
(c) neighbours of cell on inner grid

Figure 5. Identification of neighbouring cells on a cylindrical sliding-plane interface between an inner grid around a blunt-nose cylinder and a coarser rotating outer grid: (a) example of overlapping cells in one of the block faces of the interface; (b) example of a cell face on the coarse patch overlapping with six neighbour cells; and (c) cell face on finer inner mesh overlapping with two cells on the outer mesh.

any metric of the block-face size can be used. For planar interfaces and highly regular block face shapes, the mean of both diagonals would suffice. This metric may have to be adjusted for block faces with highly stretched grids.

To check the potential of cell overlap, a search range is used which is based on the diagonals of the cells considered. For cells within this interaction radius, the cell face overlap computation is performed. The overlap computation can handle quadrangles of arbitrary shapes and involves checks for a range of overlap patterns.

Without the interaction radius checks, the neighbour identification for a sliding-plane interface with N_1 cells along the interface on one side and N_2 cells on the other side would involve $N_1 \times N_2$ overlap computations. The construction of the neighbour block face list reduces the computational overhead. Although the cost of the above process remains $O(N_1 \times N_2)$, it copes with complex configurations such as the rotor–fuselage cases. For the cases considered in the present work, the implemented identification method was found to have an acceptable computational overhead. For the generic demonstration cases, the overhead was as little as 1–2% of the simulation time. For the more complex rotor–fuselage test cases, with significantly larger mesh sizes, the simulation needs to be performed in parallel, leading to a more complex identification process. This problem was addressed by developing a separate parallel pre-processor for identification and interpolation weight computation, which is described in the following section.

3.3. Parallelization of the method

The present implementation of the sliding-mesh method was designed for execution on a distributed-memory multi-processor computer, typically a low-cost Linux cluster. The method is embedded in the HMB flow solver, which, for parallel simulations on distributed-memory computers, divides the sub-domains between processors, each of which stores only the flow field data and the mesh for the assigned sub-domains. In the neighbour-identification step, the mesh coordinates for cells along neighbouring block faces are required. The main challenge in the parallel execution arises from the fact that the neighbouring block may be assigned to a different processor and, therefore, the required mesh coordinates will not be readily available. Furthermore, if the grids bordering the sliding-plane interface are moving, the multi-block topology is a function of time, and therefore the communication pattern required for the neighbour identification step will vary for each time step.

In the design of the parallel implementation of the neighbour-identification and weight-computation steps, the main challenge is to limit the number of message-passing communications and the amount of communicated data. In the present approach, a parallel pre-processor performs the neighbour identification as well as the determination of the interpolation weights. For each time step in the flow simulation, the pre-processor creates a file containing, for each cell on the sliding-plane interface, a list of the neighbouring cells and corresponding weights. For each cell, its block index and the indices of the neighbouring cells on the other side of the sliding plane are stored. This out-of-core computation is necessary for large grids where storage of the whole grid on each processor during parallel execution is not possible.

Parallel computations also require an efficient approach to exchange flow field data among the processors which have one or more blocks assigned on the sliding plane. The parallel execution of the sliding-plane method is illustrated in Figure 6 for a simple example with a 10-block mesh distributed over four processors. A two-dimensional case is shown for clarity. In the parallel execution, a parameter $n_{\mathrm{CPU,SP}}$ defines the number of processors used to store the blocks adjacent to

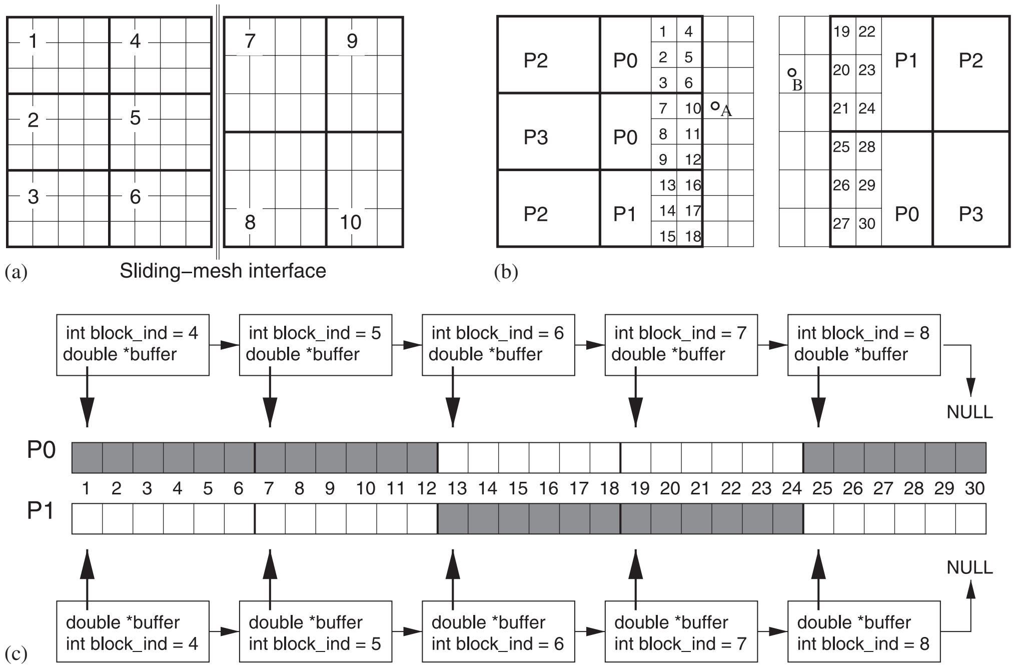

Figure 6. Example of parallel execution of a 10-block mesh on four CPUs. Processors 0 and 1 share the blocks along the sliding-mesh interface, whereas 3 and 4 receive the remaining blocks. Processors 0 and 1 allocate a buffer to store two cell layers of data along the interface. Collective broadcast operations distribute the buffer data: (a) 10-block mesh; (b) processor assignment and cell indices in buffer; and (c) sliding-plane face list and buffer construction on two CPUs.

the sliding-plane interface ($n_{\text{CPU,SP}} = 2$ in the example). The parallel execution of the sliding-plane method in the flow solver involves the following steps:

1. *Load balancing*: In this step, sub-domains having one or more faces along the sliding-plane interface are identified. These sub-domains are assigned to the first $n_{\text{CPU,SP}}$ processors, whereas the rest are assigned to the remaining processors. Among both batches of processors, the computational load is evenly distributed by a process in which the least loaded processor is given additional blocks until all blocks are distributed. In the present MPI-based implementation, an `MPI_Communicator` is created for the 'sliding-plane' processors. This communicator enables collective communications among the 'sliding-plane' processors, while the default `MPI_Communicator`, i.e. `MPI_Comm_World`, is used for collective communications between all processors.
2. *Sliding-plane buffer allocation*: In this process, a linked list is constructed, in which each list element holds the following: (i) the block index, (ii) block face index, (iii) a pointer to the part of the flow solution buffer for this block (i.e. `buffer` in Figure 6(c)) and (iv) the size of this part of the buffer. The flow solution buffer contains the flow field variables for the two layers of cells adjacent to the sliding-plane interface. The need to store just two layers of cell data means that the memory allocated on each processor for the buffer is low. It should

be noted that although the stride in the buffer index for adjacent cells is one in Figure 6, the stride used in the flow solver equals the number of unknowns per cell. The list contains elements for each of the block faces on the sliding-plane interface and is allocated on each of the first $n_{\mathrm{CPU,SP}}$ processors. In Figure 6, the list has five entries. The cell indices of the neighbours pre-computed by the pre-processor are actually the indices of neighbour cells in this buffer.

3. *Sliding-plane weights allocation*: In this step, a `weights` data structure is allocated for each cell of the locally allocated blocks on the sliding-plane interface. The `weights` data type holds (i) the number of neighbour cells, (ii) a variable-length array storing the block index, (iii) the cell index and (iv) the weight for each neighbour cell.
4. *Sliding-plane buffer update*: This update consists of two steps. First, each processor copies the most recent flow solution data into the flow solution buffers of the blocks assigned to that processor. Figure 6 shows the parts of the buffer stored on each processor before data communication. The blank entries in the buffer shown in the sketch indicate the parts which need to be received from other processors. Collective broadcast (`MPI_Bcast`) operations using the dedicated sliding-plane `MPI_Communicator` are used to update the remaining flow solution buffer entries on each of the first $n_{\mathrm{CPU,SP}}$ processors.
5. *Sliding-plane weights update*: In this step, the weights file created in the pre-processing stage is read by each one of the first $n_{\mathrm{CPU,SP}}$ processors. On each processor, only the relevant interpolation data are stored.

Steps (4) and (5) are repeated at the end of each pseudo-time step (m in Equation (4)). Following the above steps, the halo values required for the block faces on the sliding plane can be obtained from the buffer data stored on each processor. For example, for halo cell A in Figure 6, only one neighbour will be used (corresponding to buffer index 21), whereas for halo cell B, the halo data are obtained from a weighted summation of buffer data at indices 2 and 3. For three-dimensional problems with non-matching stretched grids, the number of neighbours will range from one to tens or even hundreds.

4. DEMONSTRATION OF THE METHOD AND DISCUSSION OF THE RESULTS

The technique described in the previous section has been implemented in HMB and tested for a variety of cases. The obtained results are presented in this section.

4.1. Flows over bumps and around aerofoils

The first test case considered was the inviscid flow over a bump. For this case, a matching multi-block grid was generated with 6400 cells, as shown in Figure 7(a). The sliding-plane grid shown in Figure 7(b) was obtained by introducing a horizontal split. The solution obtained with the inter-block boundary treated as a normal block boundary is shown in Figure 7(c). The sliding-plane solution is shown in Figure 7(d). The comparison shows that there is no difference between the obtained results and this suggests that the existing interpolation method did not introduce any numerical artefacts. This was expected since both sides of the sliding plane had matching grids. Owing to the small size of the employed grid, the computational overhead for the case where the sliding-plane algorithm is used is very low. Profiling of the solver revealed an increase of less than

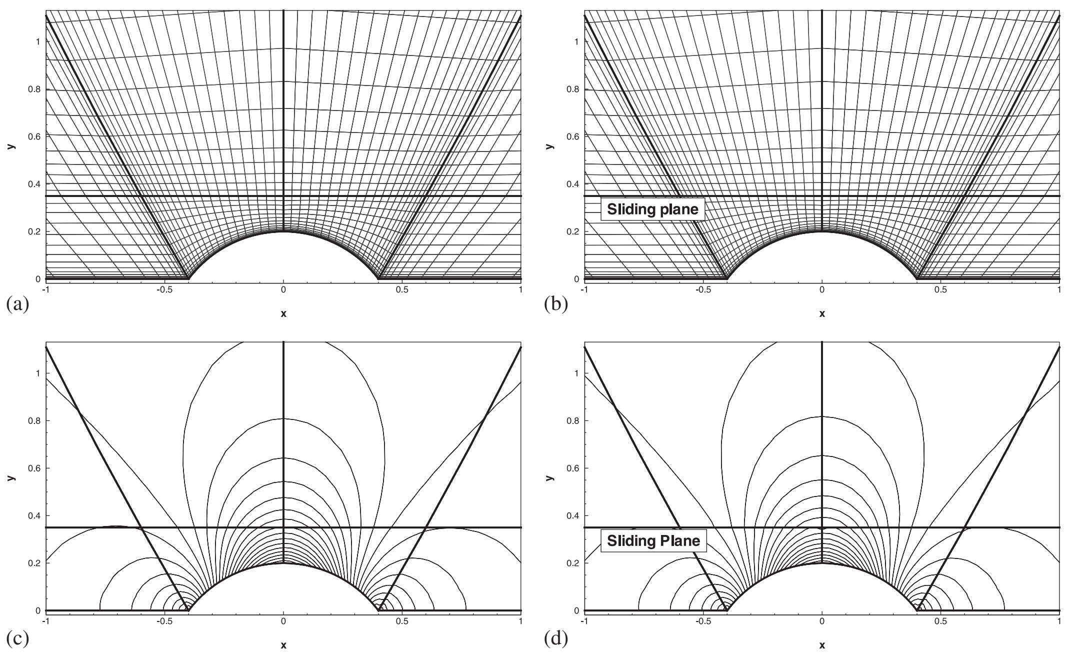

Figure 7. Inviscid subsonic flow over circular bump ($M_\infty = 0.40$). (a) An 8-block matching multi-block grid is used, which for the sliding-plane test is split along the horizontal line indicated in (b). (a) Matching multi-block mesh; (b) matching patched mesh; and (c) and (d) pressure distribution.

1% of CPU time. A small number of iterations, about 200, were needed for convergence and a CFL of 25 was used for the implicit time marching.

A second test case attempted was the transonic inviscid flow around the ONERA213 airfoil, shown in Figure 8. For this case, a multi-block grid was generated (see Figure 8(a)), which formed the basis for two sliding-plane grids: a matching grid with the sliding-plane interface wrapped around the upper half of the airfoil at a distance of 0.5 of the chord length (Figure 8(b)) and a non-matching grid, obtained by refining the blocks within the sliding-plane interface by 50% in the chord-wise direction (Figure 8(c)). The multi-block grid shown in Figures 8(a) and (b) has 40 cells in the wall-normal direction, 170 in the wrap-around direction and 30 in the stream-wise direction in the wake. The wall spacing of the first cell is 10^{-3} of the chord. The non-matching grid shown in Figure 8(c) has 125 cells in the wrap-around direction on the upper surface instead of 85 in the baseline grid. The iso-bars of the solutions for a free-stream Mach number of 0.75 for the three cases are shown in Figures 8(d)–(f). The comparison shows no difference between the results obtained with the standard multi-block formulation and the matching-grid sliding plane, whereas the non-matching sliding-plane case shows a reduction in the shock thickness in the refined grid blocks. Again, this was expected. In comparison with the previous test case, the sliding plane is now curved and the interpolation is harder. In addition, significant flow gradients are now present. Less than 300 iterations were necessary for convergence to be obtained and a CFL number of 15 was used. The refinement technique enabled by the use of a sliding-plane interface opens possibilities for reducing the number of cells required to obtain an accurate solution compared

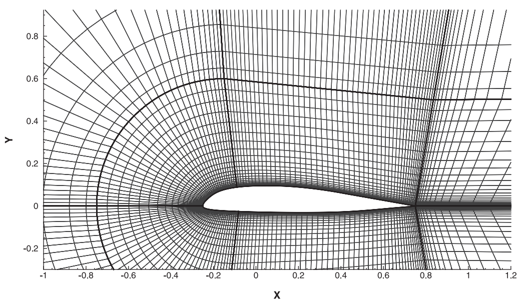

(a) Matching multi-block mesh

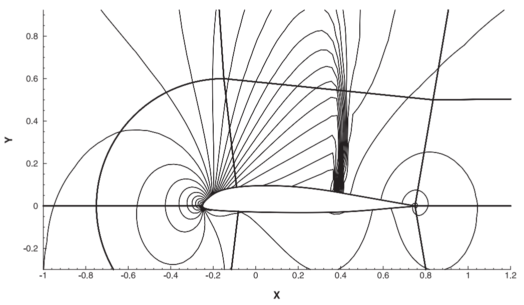

(d) Pressure distribution

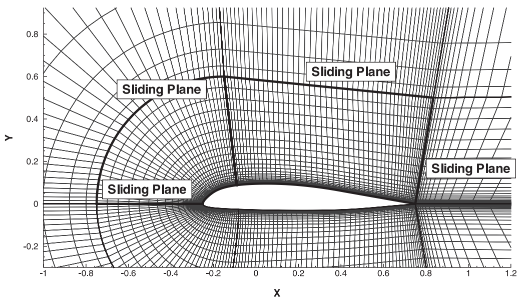

(b) Matching patched mesh

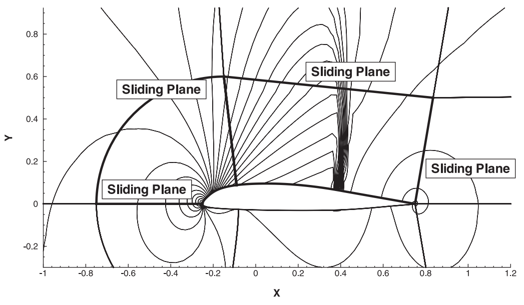

(e) Pressure distribution

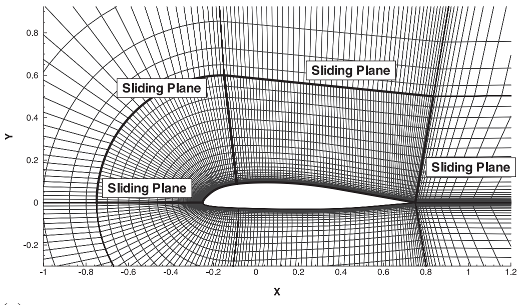

(c) Non-matching patched mesh

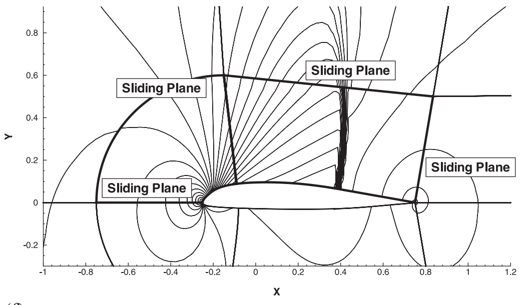

(f) Pressure distribution

Figure 8. Transonic inviscid flow around ONERA OA213 airfoil (2° incidence, $M_\infty = 0.75$): (a) and (b) mesh and pressure distribution obtained with regular multi-block formulation; (c) and (d) continuous grids matched along a multi-segment curved sliding-plane interface; and (e) and (f) non-continuous grids obtained by refining the leading-edge and upper surface blocks.

with normal multi-block grids. For the present case, the overhead in terms of CPU time due to the presence of the sliding plane was less than 1%.

The third test case considered here is the transonic flow around the ONERA213 airfoil with shock-induced separation of the boundary layer. Again, the free-stream Mach number is 0.75, whereas the incidence has been increased to 8°. The simulations for these conditions used the two-equation *k*–*ω* turbulence model, for a Reynolds number, based on the chord length, of 1 million. The multi-block meshes and the obtained results are presented in Figure 9. The mesh topology is

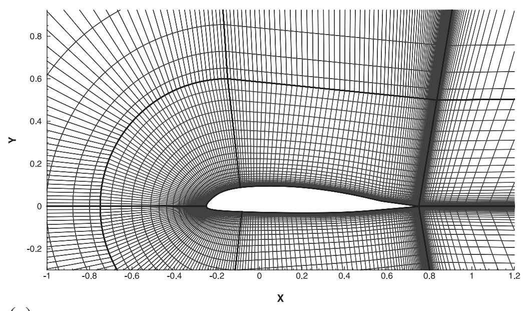

(a) Matching multi-block mesh

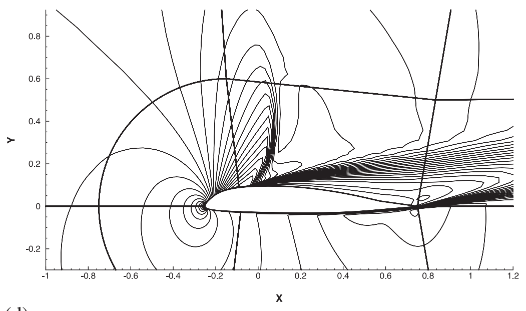

(d) Mach number

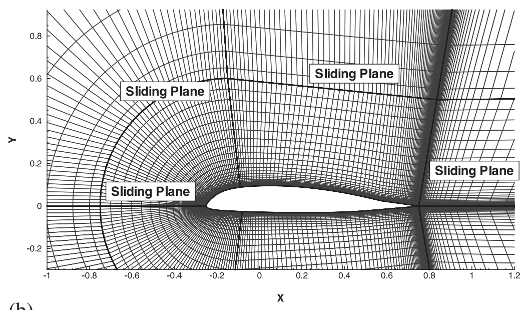

(b) Matching patched mesh

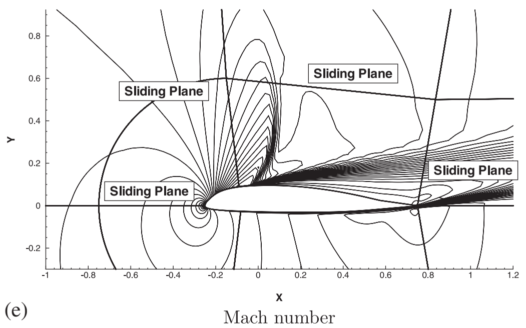

(e) Mach number

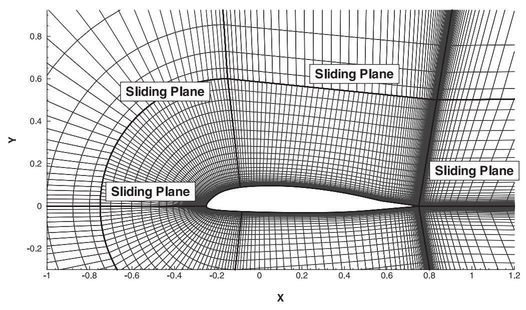

(c) Non-matching patched mesh

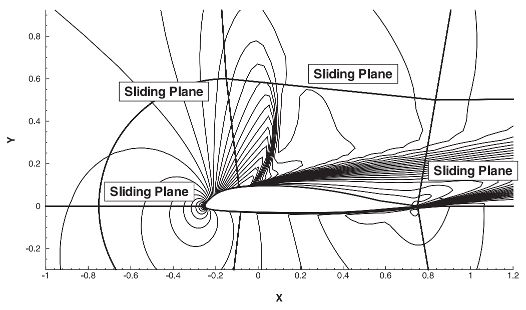

(f) Mach number

Figure 9. Transonic turbulent flow around ONERA OA213 airfoil (8° incidence, $M_\infty = 0.75$), with shock-induced boundary layer separation: (a) and (b) mesh and pressure distribution obtained with regular multi-block formulation; (c) and (d) continuous grids matched along a multi-segment curved sliding-plane interface; and (e) and (f) non-continuous grids obtained by coarsening blocks outside sliding-plane interface by 50% in chord-wise direction.

identical to that for the previous inviscid test case. The number of cells in the wall normal direction has been increased from 40 to 65 while the wall spacing of the first cell is reduced from 1×10^{-3} to 0.5×10^{-5} of the chord. The multi-block grid shown in Figures 9(a) and (b) has 250 cells in the wrap-around direction and 45 in stream-wise direction in the wake. The non-matching grid shown in Figure 9(c) has a reduced number of cells in the wrap-around direction in the blocks outside the sliding-plane interface. The number of cells in this direction is reduced from 250 to 170, whereas

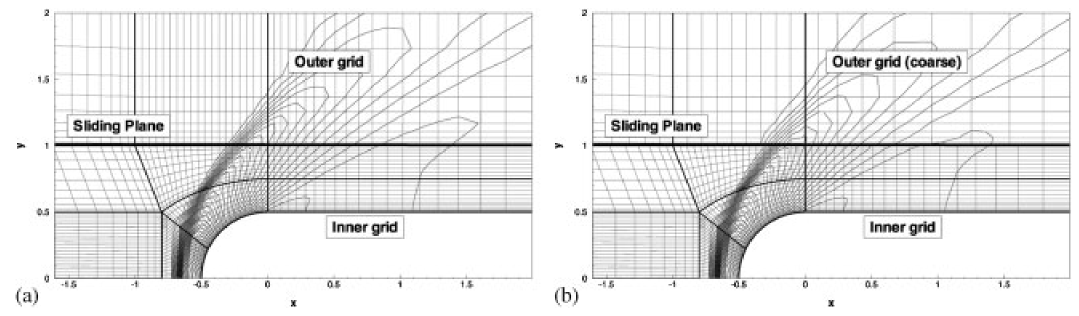

Figure 10. Supersonic inviscid flow around blunt cylinder (0° incidence, $M_\infty = 2.0$): (a) mesh and pressure distribution obtained with regular multi-block formulation and (b) non-matching mesh and pressure distribution obtained with sliding-plane method. The non-continuous grid was obtained coarsening the outer grid.

the grids in the two blocks on the upper surface maintain the same number of cells as the baseline grid. As in the previous inviscid example, the sliding-plane method was used to simulate the flow on a matching patched grid as well as a non-matching grid. The results are compared with results for the conventional multi-block formulation in Figures 9(d)–(f). In this example, the sliding plane intersects the boundary layer in the leading-edge normal direction as well as in the wall normal direction at the trailing edge on the upper surface of the airfoil. It can be seen that the sliding-plane interpolations do not introduce numerical artefacts for this test case.

As a final demonstration case, the supersonic flow around a blunt-nose cylinder was considered. The multi-block topology and the location of the sliding-plane interface were previously shown in Figure 5 and discussed in Section 3.2. This example was designed to test the sliding-plane algorithm for curved three-dimensional interfaces with significant flow gradients, i.e. the bow shock found around the cylinder. The results for the inviscid flow at free-stream Mach number 2.0 are shown in Figure 10(a) for a matching grid and in Figure 10(b) for a non-matching grid obtained by coarsening the outer mesh. As in the previous example, the sliding-plane interface did not introduce any numerical artefacts. The only significant effect of the coarsened outer grid is the spreading of the bow shock wave, while the solution on the inner grid is not affected.

4.2. Rotor–fuselage test cases

The first rotor–fuselage test case involves the ROBIN model helicopter model [1, 2, 24]. The overall configuration is shown in Figure 11(a). The four-blade rotor has an aspect ratio of 13 and consists of a NACA0012 section, with a linear twist of 8°. In the experimental set-up, the rotor is suspended from the wind-tunnel roof, while the fuselage has a floor-mounted wind-tunnel support. Both supporting structures are omitted in the geometry used here. The rotor hub is modelled as an ellipsoidal surface. The geometry includes the 2-in rotorshaft offset from the fuselage centreline and the 3° forward tilt of the rotor shaft. Figure 11(b) shows the locations of the surface pressure taps and inflow measurements from the NASA experiments which are used here. The test case considered here has a rotor tip Mach number of 0.5, the advance ratio is 0.15 and the rotor thrust coefficient was $C_T/\sigma = 0.0656$ in the experiment. The rotor trim state is that reported by Park *et al.* [13], with collective, longitudinal and lateral cyclic pitch angles of 6.0, −2.2 and −2.0°, respectively. The inviscid flow simulations were conducted on multi-block-structured grids with

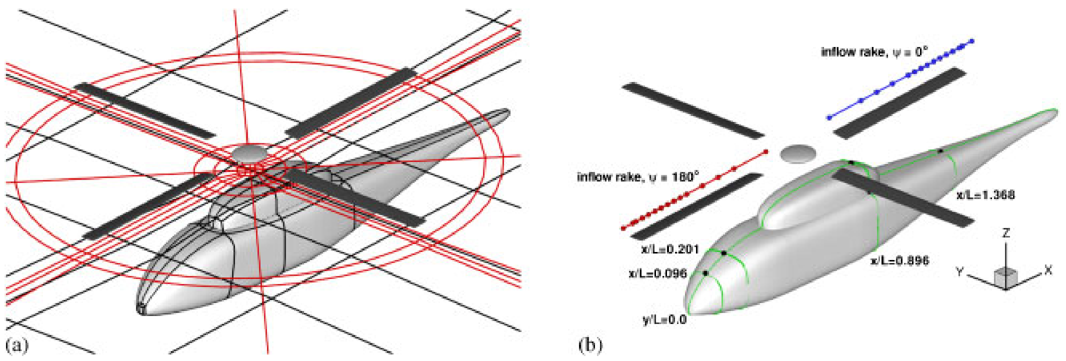

Figure 11. ROBIN configuration used in the present CFD study. The wind tunnel supports for the floor-mounted fuselage and the roof-mounted rotor are omitted: (a) sliding-mesh interface is located 1.0 blade chord below the rotor disk and (b) location of pressure taps and inflow measurements used in the present work.

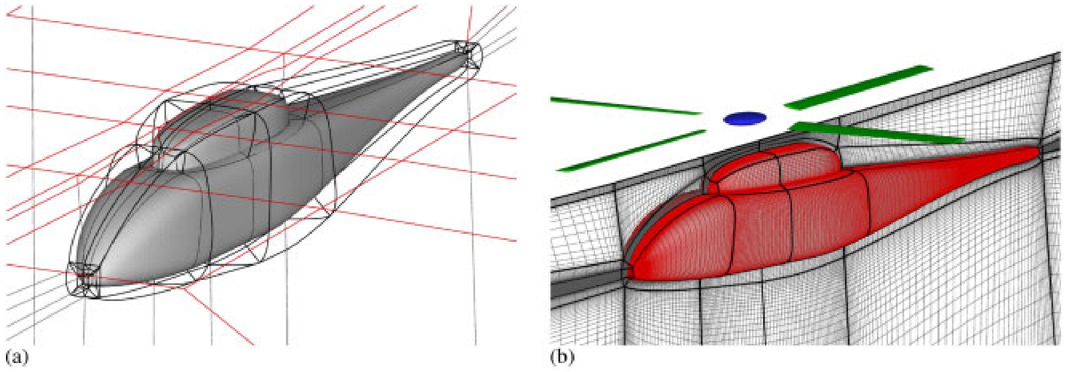

Figure 12. Multi-block topology for ROBIN configuration. Around the fuselage, an O-topology is used with a high degree of surface orthogonality: (a) fuselage and symmetry plane topology and (b) fuselage and symmetry plane mesh.

the sliding-plane interface located one blade chord below the rotor disk. The fuselage grid has an O-type topology in the direct vicinity of the fuselage, embedded in a domain with a cylindrical side surface, with the same diameter as the rotor grid far-field boundary, and an upper surface orthogonal to the rotor shaft. The grid has 240 blocks and 4.0×10^6 cells. The topology and mesh are shown in Figure 12. The rotor grid has a C-H topology, with 456 blocks and 5.5×10^6 cells. The rotor grid has 50 cells in the span-wise direction of each blade, 45 cells in the surface normal direction, 150 cells around the blade chord and 40 cells in the stream-wise direction between the blades. The simulation was run for four rotor revolutions using azimuthal steps of 1.0°. For the fourth rotor revolution, the thrust coefficient was $C_T/\sigma=0.0066$, which is within 0.6% of the value for the third revolution, indicating a sufficient level of convergence, confirmed by surface pressure plots for the third and fourth revolutions discussed later. The neighbour searches and interpolation weights were pre-computed with the pre-processor discussed in Section 3.3, requiring about 5% of the total CPU time. The sliding-plane method added an additional 5–6% communication overhead for the parallel simulation conducted on 40 Pentium four processors of a Linux cluster. The grid blocks along the sliding-plane interface were allocated to the first six processors, i.e. the parameter $n_{\mathrm{CPU,SP}}$ defined in Section 3.3 was set to 6.

Figure 13 compares the time-averaged induced flow field components in the stream-wise and rotor-disk normal direction from the experiment [25] with CFD data averaged over one rotor revolution. The agreement is favourable, with a slight over-prediction of the stream-wise component. This is an encouraging result, since any loss of continuity across the sliding plane would have an effect on the obtained velocity field.

Time-averaged surface pressure coefficients are shown in Figure 14 for the cross sections $x/L=0.35$ and 1.17. The small discrepancy at the lower surface for $x/L=1.17$ can be (partly) attributed to the absence of the wind-tunnel support in the CFD geometry. Figure 15 shows the unsteady pressure distribution for four rotor azimuth positions. In the figure, the revolution-averaged pressure coefficient has been subtracted from the instantaneous pressure coefficients. At $\psi=90°$, the blade at the front and back of the rotor disk crosses the fuselage centreline. A positive pressure change leads this blade passing, while the maximum pressure occurs 5–10° after the centreline passing. After the passage, a negative change to the average pressure occurs, which is particularly notable behind the fuselage fairing in the plot for $\psi=110°$ in Figure 14. Figure 16 compares the predicted

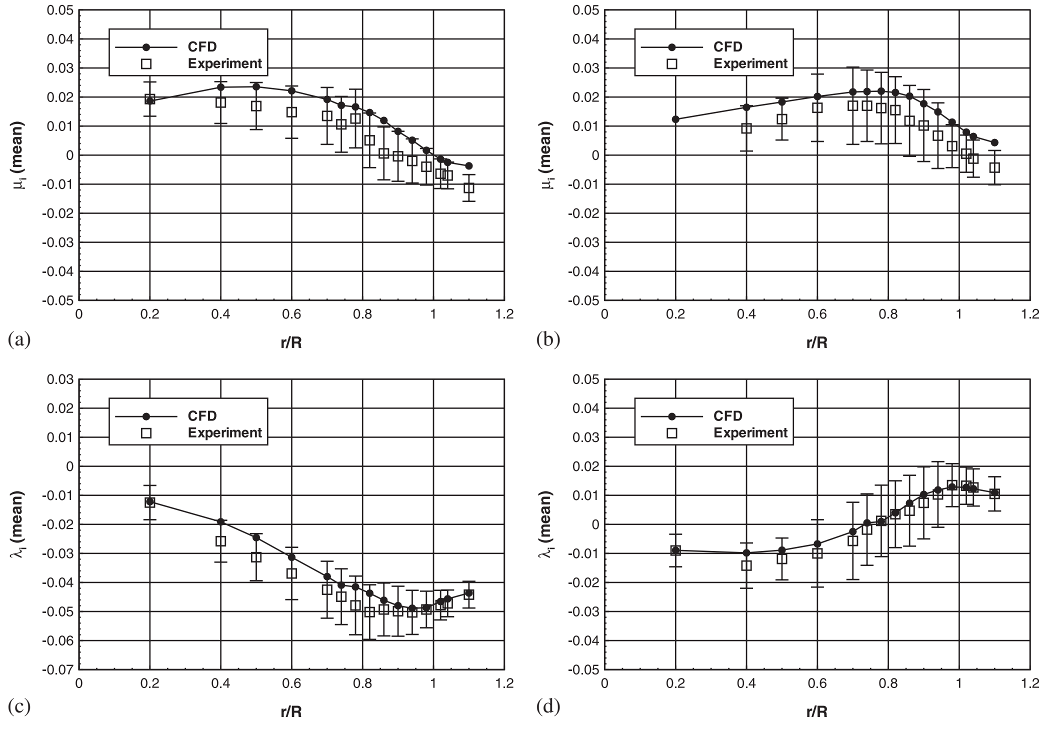

Figure 13. In-plane (μ_i) and normal (λ_i) velocity ratios at 0° (a, c) and 180° (b, d) azimuth angles. The velocity was extracted above the rotor disk plane at $z/c=1.1$. The thrust coefficient was $c_{\mathrm{T}}=0.0065$, $M_{\mathrm{tip}}=0.51$, advance ratio $\mu=0.15$.

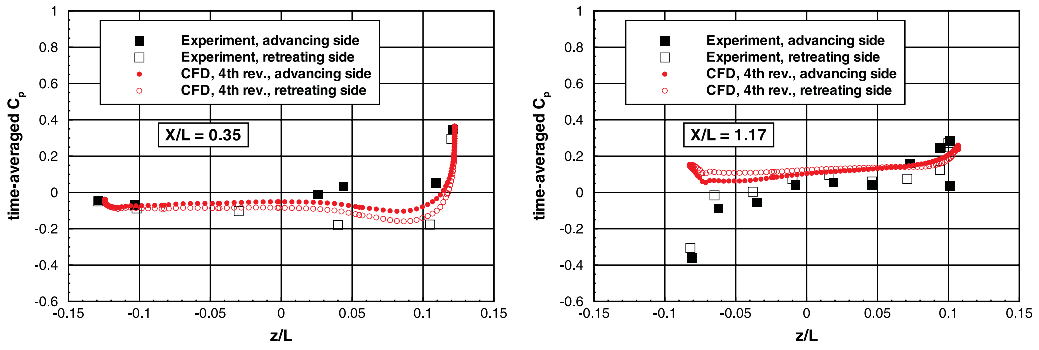

Figure 14. Time-averaged surface pressure coefficient for ROBIN configuration. Thrust coefficient $c_T = 0.0065$, $M_{\text{tip}} = 0.51$, advance ratio $\mu = 0.15$.

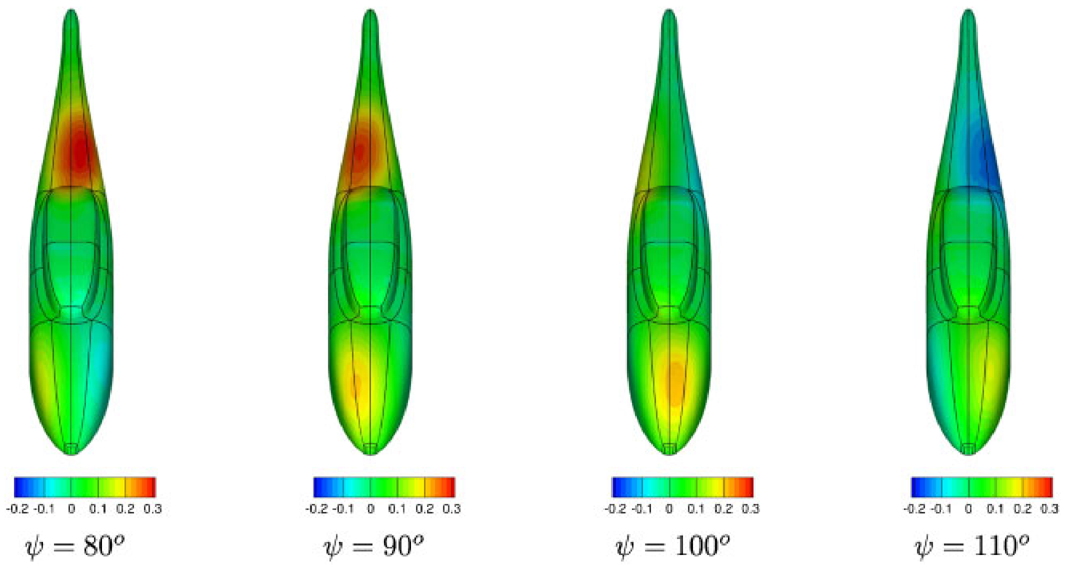

Figure 15. Unsteady surface pressure distribution for ROBIN test case. In the plots, the revolution-averaged pressure coefficient has been subtracted from the instantaneous surface pressure coefficient to highlight the blade-passing effect on the pressure field.

time-dependent surface pressure coefficients with the experimental data [24]. The pressure in the four centreline positions defined in Figure 11(b) is shown in Figures 16(a)–(d). The pressure in probe locations on the side of the fuselage fairing is shown in Figures 16(e) and 16(f), for the retreating and advancing sides of the rotor, respectively. The peak-to-peak pressure fluctuations agree favourably with the experiment, while a consistent phase shift relative to the experimental data is present. This phase shift corresponds to that found previously by Park *et al.* [13]. Their solution for this test case is also plotted on the same figure.

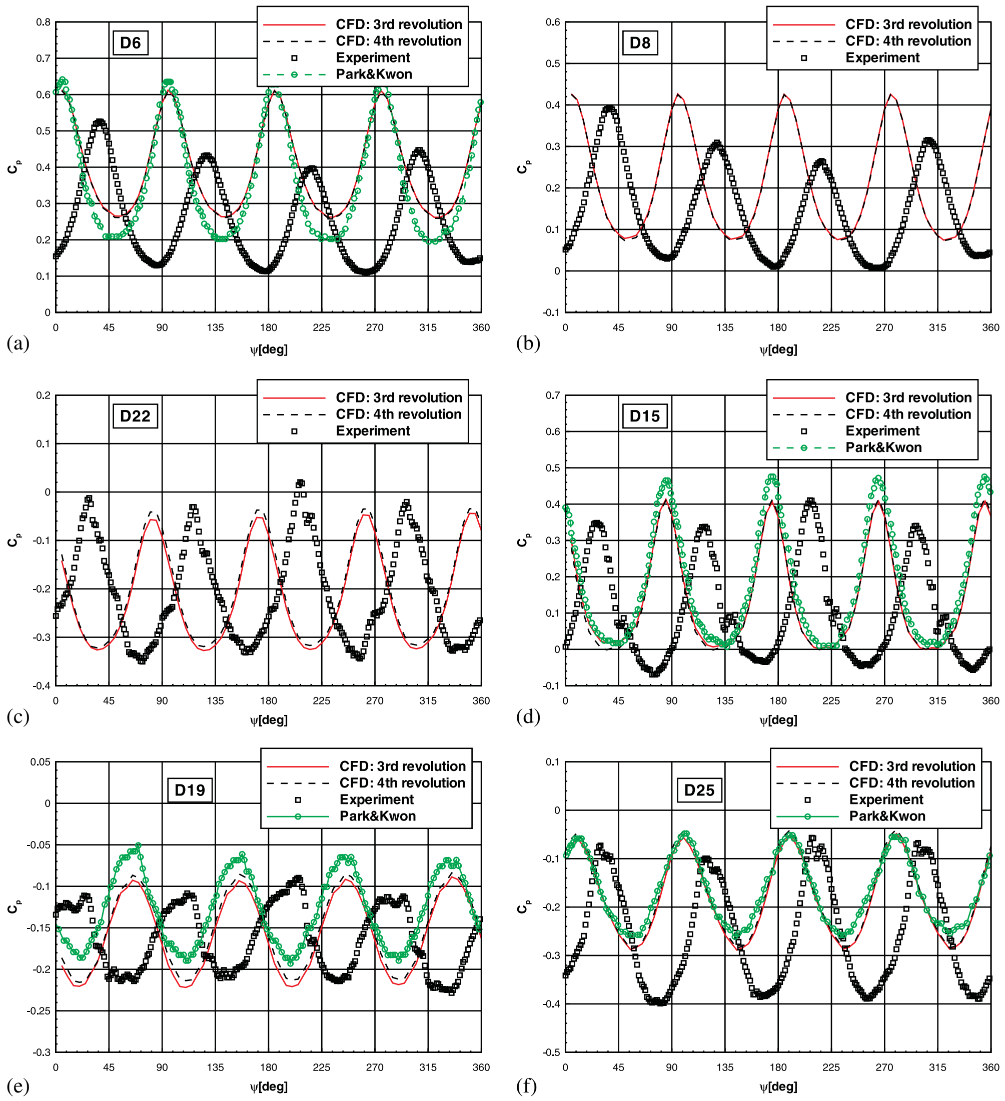

Figure 16. Surface pressure distribution for ROBIN test case: (a) centreline, $x/L=0.096$; (b) centreline, $x/L=0.201$; (c) centreline, $x/L=0.896$; (d) centreline, $x/L=1.368$; (e) $x/L=0.896$, $y/L=-0.07$, $z/L=0.125$; and (f) $x/L=1.368$, $y/L=0.07$, $z/L=0.125$.

A second rotor–fuselage test case demonstrates the capability of the method to handle more complex, realistic helicopter geometries. The case considered here is the wind-tunnel model of a medium-weight generic helicopter with the four-bladed ONERA 7AD rotor, equipped with anhedral tips and parabolic taper. This configuration is under investigation for the GOAHEAD EC Sixth Framework Research Project. The geometry and the multi-block topology are shown in Figure 17. The multi-block mesh for the fuselage has 1624 blocks and approximately 6.5×10^6 cells, whereas

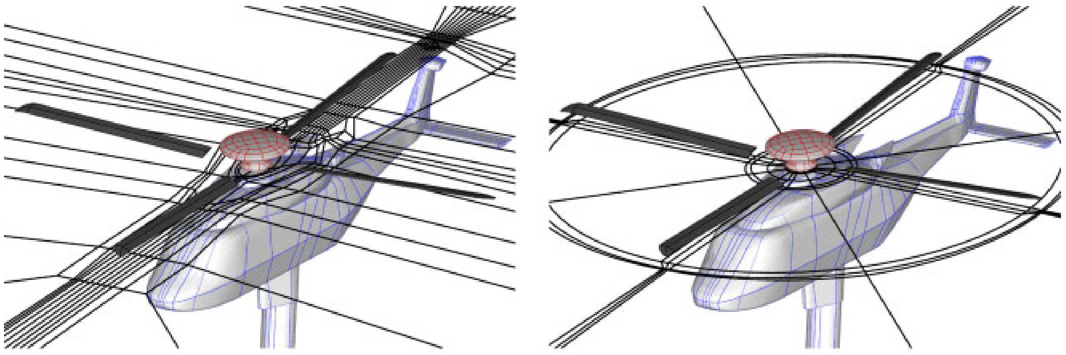

Figure 17. Geometry and multi-block topologies for a realistic helicopter model.

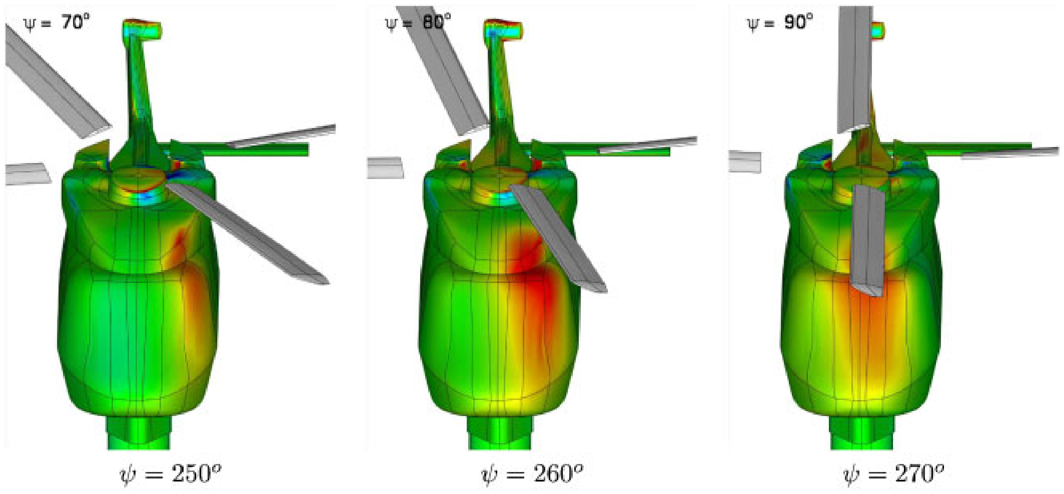

Figure 18. Unsteady surface pressure distribution for the helicopter model of Figure 17, in forward flight at different rotor azimuth angles. In the plots, the revolution-averaged pressure coefficient has been subtracted from the instantaneous surface pressure coefficient to highlight the blade-passing effect on the pressure field.

the rotor mesh has 856 blocks and 4.1×10^6 cells. The rotor shaft is mounted on the fuselage with 5° forward inclination. The case considered corresponds to an economic cruise condition, for which the free-stream Mach number is 0.204 and the tip Mach number of the rotor is 0.62. A representative rotor trim schedule is used in the simulation, i.e. the rotor has a cyclic pitch change as well as a harmonic blade flapping. The rotor multi-block topology is designed to handle the grid deformation as discussed in Reference [17]. This test case was run in parallel on 96 Pentium four processors, where the blocks with a face on the sliding-plane interface were stored on the first 16 processors. The simulations were run for three rotor revolutions with a time step corresponding to 0.25° rotor rotation and the k–ω turbulence model was used. The effect of the blade passing on the surface pressure distribution of the front part of the fuselage is shown in Figure 18, where the pressure pattern near the stagnation point formed at the front of the fuselage is altered every time a blade is passing above. This test case represents a realistic helicopter configuration and further proves the ability of the proposed method to cope with complex multi-block topologies.

5. SUMMARY AND FUTURE WORK

A CFD technique was presented which allows CFD computations on grids with non-matching cell faces. The main application of the method is the analysis of rotor–fuselage configurations though other configurations are possible. Results have been presented for several flow cases including simple two-dimensional flows and even complete rotor–fuselage configurations. The obtained results suggest that the proposed method is adequate in terms of both accuracy and efficiency. The overhead of the method in terms of CPU time was found to be almost proportional to the size of the employed grid. Issues regarding the parallel efficiency of the method had to be addressed since a substantial amount of information must be communicated between processors sharing blocks with faces on sliding planes. Further, the proposed search algorithm takes no advantage of the prescribed rotational motion of the rotor and it is expected that further savings in CPU time can be obtained by narrowing the search radius according to the employed grid and time step. In the future, more advanced methods will be investigated, such as the method described in Reference [5] and random walk search methods to allow further reductions in the overhead associated with the sliding-plane method.

ACKNOWLEDGEMENTS

During the preparation of this paper, R. Steijl was supported by the European Union under the Integrating and Strengthening the European Research Area Programme of the 6th Framework, Contract number 516074 (GOAHEAD project).

REFERENCES

1. Freeman CE, Mineck RE. Fuselage surface pressure measurements of a helicopter wind-tunnel model with a 3.15-meter diameter single rotor. *NASA TM-80051*, 1979.
2. Chaffin MS, Berry JD. Navier–Stokes and potential theory solutions for a helicopter fuselage and comparison with experiment. *NASA TM-4566*, June 1994.
3. Rai M. A conservative treatment of zonal boundaries for Euler equation calculations. *Journal of Computational Physics* 1986; **62**:472–503.
4. Rai M. A relaxation approach to patched-grid calculations with the Euler equations. *Journal of Computational Physics* 1986; **66**:99–131.
5. Barakos G, Vahdati M, Sayma AI, Breard C, Imregun M. A fully distributed unstructured Navier–Stokes solver for large-scale aeroelasticity computations. *The Aeronautical Journal* 2001; **105**:419–426.
6. Osher S, Chakravarthy S. Upwind schemes and boundary conditions with applications to Euler equations in general geometries. *Journal of Computational Physics* 1983; **50**:447–481.
7. Steger JL, Warming RF. Flux vector splitting of the inviscid gasdynamics equations with application to finite-difference methods. *Journal of Computational Physics* 1981; **40**:263–293.
8. Eliasson P, Wand D, Meijer S, Nordström J. Unsteady Euler computations through non-matching and sliding-zone interfaces. *Thirty-sixth Aerospace Sciences Meeting and Exhibit*, Reno, U.S.A., 12–15 January 1998; AIAA Paper 1998-0371.
9. Pahlke K, Van der Wall B. Calculation of multibladed rotors in high-speed forward flight with weak fluid–structure-coupling. *Twenty-seventh European Rotorcraft Forum*, Moscow, Russia, September 2001.

10. Renaud T, Benoit C, Boniface J-C, Gardarein P. Navier–Stokes computations of a complete helicopter configuration accounting for main and tail rotor effects. *Twenty-ninth European Rotorcraft Forum*, Friedrichshafen, Germany, September 2003.
11. Pomin H, Wagner S. Aeroelastic analysis of helicopter rotor blades on deformable chimera grids. *Journal of Aircraft* 2004; **41**(3):577–584.
12. Potsdam M, Yeo W, Johnson W. Rotor airloads prediction using loose aerodynamic/structural coupling. *American Helicopter Society 60th Annual Forum*, Baltimore, MD, 7–10 June 2004.
13. Park Y, Nam HJ, Kwon OJ. Simulation of unsteady rotor–fuselage aerodynamic interaction using unstructured adaptive meshes. *Fifty-ninth Annual Forum of the American Helicopter Society*, Phoenix, AZ, 6–8 May 2003.
14. Park Y, Kwon OJ. Simulation of unsteady rotor flow field using unstructured adaptive sliding meshes. *Journal of the American Helicopter Society* 2004; **49**(4):391–400.
15. Nam HJ, Park Y, Kwon OJ. Simulation of unsteady rotor–fuselage aerodynamic interaction using unstructured adaptive meshes. *Journal of the American Helicopter Society* 2006; **51**(2):141–148.
16. Barakos G, Steijl R, Badcock K, Brocklehurst A. Development of CFD capability for full helicopter engineering analysis. *Thirty-first European Rotorcraft Forum*, Florence, Italy, 13–15 September 2005.
17. Steijl R, Barakos G, Badcock K. A framework for CFD analysis of rotors in hover and forward flight. *International Journal for Numerical Methods in Fluids* 2006; **51**:819–847.
18. Steijl R, Barakos G. CFD analysis of rotor–fuselage interactional aerodynamics. *Forty-fifth AIAA Aerospace Sciences Meeting and Exhibit*, Reno, Nevada, U.S.A., 8–11 January 2007; AIAA Paper 2007-1278.
19. Badcock K, Richards B, Woodgate M. Elements of computational fluid dynamics on block structured grids using implicit solvers. *Progress in Aerospace Sciences* 2000; **36**(5–6):351–392.
20. Jameson A. Time dependent calculations using multigrid, with applications to unsteady flows past airfoils and wings. *AIAA Paper*, *91-1596*, 1991.
21. Morvant R, Badcock K, Barakos G, Richards BE. Aerofoil–vortex interaction using the compressible vorticity confinement method. *AIAA Journal* 2004; **43**(1):63–75.
22. Spentzos A, Barakos G, Badcock K, Richards BE, Wernert P, Schreck S, Raffel M. CFD investigation of 2D and 3D dynamic stall. *AIAA Journal* 2005; **34**(5):1023–1033.
23. Van Albada GD, van Leer B, Roberts WW. A comparative study of computational methods in cosmic gas dynamics. *Astronomy and Astrophysics* 1982; **108**:76–84.
24. Mineck RE, Althoff Gorton S. Steady and periodic pressure measurements on a generic helicopter fuselage model in the presence of a rotor. *NASA TM 210286*, 2000.
25. Elliot JW, Althoff SL, Sailey RH. Inflow measurements made with a laser velocimeter on a helicopter model in forward flight, Volume 1, Rectangular planform blades at an advance ratio of 0.15. *NASA TM 100541*, 1988.